





Comparison of different atmospheric phase screen correction models in ground-based radar interferometry for landslide and open-pit mine monitoring

Bingquan Li , Wenliang Jiang , Yongsheng Li, Yi Luo, Qisong Jiao, Xin Wang and Jingfa Zhang

National Institute of Natural Hazards, Ministry of Emergency Management of China, Beijing, China

ABSTRACT

Although the atmospheric compensation models developed to date have been generally robust and effective for InSAR, how to choose the right atmospheric correction method for ground-based InSAR is worth studying. This paper uses different methods for atmospheric phase screen (APS) compensation based on studies of ground-based radar (GBR) to zero-baseline acquisitions over the Woda landslide in Sichuan, China. This landslide has a steep topography, thick fog, turbulent rivers and strong rains. Data were acquired at the Ku-band using a GAMMA Portable Radar Interferometer II (GPRI-II) in multiple campaigns (4 July 2019–13 July 2019). In 2019, the Miyun open-pit mine was also studied; the maximum deformation reached 4.03 mm/hour. The collected data were processed within one unit based on the small baseline set (SBAS) approach. The experimental results show the following (1) For long-distance monitoring with complex atmospheric disturbances, range- and/or height-dependent models fail. (2) The iterative decomposition (ITD) method can effectively address complex atmospheric disturbances. (3) If the threshold of wavelength is set to be large, the ITD method becomes a stratified model.

ARTICLE HISTORY

Received 2 October 2020
Accepted 11 May 2021

1. Introduction

Currently, spaceborne synthetic aperture radar (SAR) is generally recognized as a powerful tool that is able to detect surface deformation and generate a digital elevation model (DEM) of an observed area by taking advantage of phase changes between SAR acquisitions (Hanssen 2001). However, the revisit period of SAR satellites restricts flexibility for deformation tasks (Pipia et al. 2012). More recently, ground-based radar (GBR) has been developed, which shows enhanced capabilities in monitoring the displacements of small areas such as dams (Wei, Qihuan, and Shunying 2016; Di Pasquale et al. 2018), bridges (Heng and Jie 2013; Zhang et al. 2018), buildings (Tarchi et al. 2000; Liu et al. 2016), and landslides (Noferini et al. 2006, 2007a; Herrera et al. 2009; Vincent, Francis, and Rajsingh 2015). Compared with spaceborne SAR, GBR has the advantages of a high stability of the

sensor platform, fine spatial resolution, no baseline error and more flexible observation angle, all within a shorter data acquisition time (Huang et al. 2015). GBR is suitable for monitoring and early warning and emergency observation, while spaceborne SAR technology is suitable for hidden danger identification and risk investigation. The application of the two methods in landslides is complementary and suitable for different application stages.

For this type of data, in addition to thermal noise and the classical sources of decorrelation, the atmospheric phase screen (APS) is the most relevant distortion to the interferometric phase that becomes directly visible in the interferograms. The APS is caused by the change in the refractive index caused by an uneven distribution of water vapour and pressure (Pipia et al. 2006; Iglesias et al. 2013; Caduff et al. 2014, 2015) in the process of radar signal propagation, which results in the change in the radar signal propagation path and velocity. Due to the appropriate revisit period and short range, GBR should be less affected by the atmosphere, but in particular environments, it is still affected. Therefore, to obtain reliable deformation maps, the atmospheric phase delay cannot be ignored because the short wavelength is sensitive to atmospheric variations in a continuous GBR campaign (Zebker, Rosen, and Hensley 1997). Other methods use external data, such as multispectral remote sensing data and meteorological model data (Eff-Darwich et al. 2012). The former method utilizes the integrated water vapour in the atmosphere provided by multispectral remote sensing data (Li 2005). The latter method can predict and simulate atmospheric conditions using analysis data (Jung, Kim, and Park 2013). Although the interferogram can be corrected using the retrieved water vapours with the two methods in InSAR processing, APS correction ground-based radar fails because of different acquisition times between auxiliary data and GBR data. When the APS reaches magnitudes and spatial extents, allowing it to completely mask the underlying signal, its stochastic properties also rely on the topography and are consequently non-constant because the APS associated with a point t is the result of an integration of different atmospheric effects along the line joining t and the instrument position (Butt, Wieser, and Conzett 2016). Hence, the APS cannot be second-order stationary, and thus widely known inference methods such as simple kriging (Cressie 1990) hold no optimality. Based on the supposed homogeneity of atmospheric parameters (humidity, temperature, and pressure), the millimetre-wave propagation model (MPM) was proposed (Liebe 1985). The model assumes that atmospheric conditions are weak for the entire monitoring site, with topographic variations along the range. However, the atmospheric parameters from a single position cannot be applied to the correction of an image corresponding to different ranges. Moreover, it is difficult to set up a meteorological instrument around the monitoring region, and the atmospheric state near the GBR is used to replace the atmospheric condition on the radar propagation path, which causes large errors.

The proposed method takes atmospheric effects, the range between the GBR and the monitoring target and the elevation into account. Efforts to correct atmospheric effects (Luzi et al. 2004) in GBR interferograms have been undertaken via two strategies: (i) range- and/or height-dependent models (Pipia et al. 2006, 2008; Iannini and Guarnieri 2010; Iglesias et al. 2013) and (ii) ITD (Li et al. 2020). However, there is no clear proposal on how to select the appropriate atmospheric correction model for different scenarios. This paper uses a multi-mode microwave interferometric radar system called the GAMMA Portable Radar Interferometer II (GPRI-II), which works at the Ku-band in the frequency range of

17.1 GHz to 17.3 GHz. To verify the applicability of the two different methods, the Woda landslide and Miyun open-pit mine were studied.

2. Related methods

Currently, there are two main strategies to correct atmospheric effects: (i) range- and/or height-dependent models and (ii) ITD. Range- and/or height-dependent models have been widely used and generally considered to be effective. These range- and/or height-dependent models fail in scenarios where strong dynamic atmospheric turbulence occurs. The ITD method can correct dynamic atmospheric variations. However, the ITD can reduce the computational efficiency. This paper mainly compares the applicability of the two strategies.

2.1. Range- and/or height-dependent models

Range- and/or height-dependent models take into account altitude and distance. The atmospheric phase is corrected by fitting the relationship among the atmospheric phase, distance and altitude. To clarify the following models, a schematic of the GBR observation geometry is displayed in Figure 1.

A simple relationship can be inferred between the atmospheric and interferometric phase variations:

$$\varphi_{atm}(\vec{r}, t) = K \times p(\vec{r}, t) \times r \quad (1)$$

where $p(\vec{r}, t) = A(t) + B(t)r$ is a function representing the atmospheric effect ($A(t)$ and $B(t)$ are coefficients), which depends on the position vector r ($r = |\vec{r}|$) and the time t (Huang et al. 2015); K is an unknown constant. If $p(\vec{r}, t)$ expansion is brought into formula (1), we obtain

$$\varphi_{atm} = a(t)r + b(t)r^2 \quad (2)$$

where $a(t) = KA(t)$ and $b(t) = KB(t)$ are coefficients.

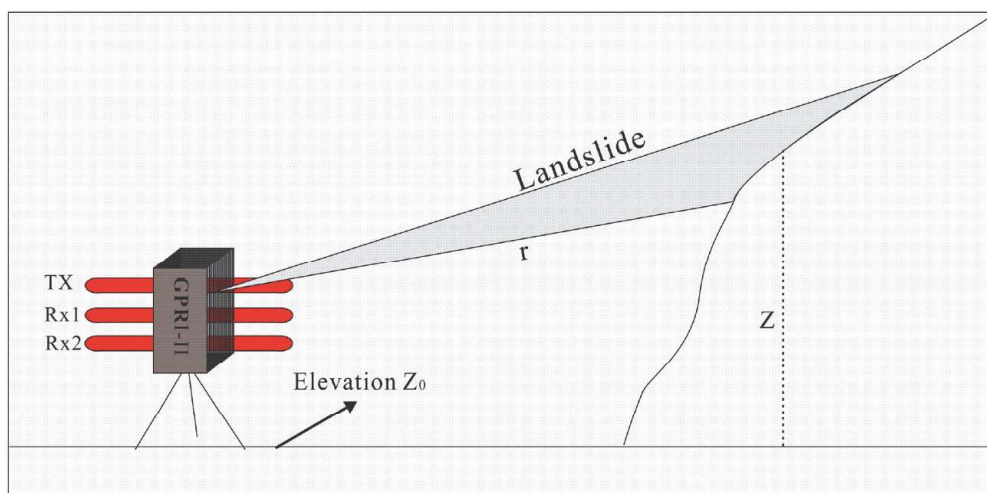


Figure 1. Schematic of the GBR observation geometry (r and z are both variables).

In mountainous areas with steep topographic variations, the assumption of spatial homogeneity might be incorrect due to changes in atmospheric parameters such as temperature, pressure, and humidity in the spatial domain. Therefore, the impact of the target area height on the atmospheric phase delay should be considered. The atmospheric phase delay is modelled as a range- and height-dependent function as

$$\varphi_{atm} = \beta_0 + \beta_1 r + \beta_2 r z \quad (3)$$

where z represents the elevation, β_0 is an offset that can appear in the differential phase between two different campaigns and β_1 and β_2 are related to the surface value of the refractivity index, the inverse of a height scale factor in km⁻¹, the time, etc. This term can be explained as the contribution of two terms: the first term increases linearly with the range, and the second term depends on the range r and the height z (Huang et al. 2015). In the horizontal direction, the APS varies linearly with the range. In the vertical direction, atmospheric conditions also vary linearly with height.

2.2. Dynamic and static APS: iterative decomposition

Range- and/or height-dependent models have been widely used for APS correction in GBR interferometry. However, if a strong dynamic APS occurs, the model fails. Thus, Wang et al. (2019) proposed a new approach for correcting static and dynamic atmospheric variations together for situations that range- and/or height-dependent models cannot address. The atmospheric variations are separated into stratified and turbulent components that are corrected iteratively in this method. In sum, atmospheric phase variations are expressed as:

$$\varphi_{atm} = \varphi_{static} + \varphi_{dynamics} \quad (4)$$

The static APS (φ_{static}) can be further divided into components: a range-dependent component $\varphi_{static_range} = \beta_0 + \beta_1 r$ and a stratified component $\varphi_{static_stratification} = \beta_2 r z$. Moreover, the range-dependent component of the static APS (φ_{static_range}) is a long-wavelength component that can be removed along with the dynamic APS ($\varphi_{dynamic}$), which behaves as long-wavelength signals. For simplicity, the sum of φ_{static_range} and $\varphi_{dynamic}$ is denoted as $\varphi_{turbulence}$, and $\varphi_{static_stratification}$ is denoted as $\varphi_{stratification}$.

$$\varphi_{atm} = \beta_2 r z + (\beta_0 + \beta_1 r + \varphi_{dynamic}) = \varphi_{stratification} + \varphi_{turbulence} \quad (5)$$

The ITD strategy for atmospheric correction of a single interferogram mainly includes the following steps: subtraction of stratification from the unwrapped interferogram and extraction of long-wavelength signals from the stratification-corrected interferogram (Corinthios 2003). The procedure of the proposed ITD strategy for atmospheric correction of a single interferogram is given as follows:

- Step 1: Mask generation of large-deformation areas.
- Step 2: Two-dimensional phase unwrapping of the interferogram.
- Step 3: Coherence estimation.
- Step 4: Regression of the stratification model using coherent pixels.
- Step 5: Subtraction of stratification from the unwrapping interferogram.
- Step 6: Extraction of long-wavelength signals from the stratification-corrected interferogram.

Step 7: Interpolation of the long-wavelength signals for the masked and low-coherent pixels.

Step 8: Subtraction of the turbulence from the stratification-corrected interferogram. The procedure stops if the iteration reaches a user-defined maximum number of iterations. Otherwise, the algorithm adds stratification to the final resultant interferogram and repeats steps 4–8.

3. Real world case studies

To verify the ability of the range elevation and ITD model to achieve atmospheric stability and strong flow and regional phase correction, the Woda landslide and Miyun open-pit mine are selected as experimental areas. The environmental characteristics of the test area are as follows (see Table 1): the monitoring distance of the Woda landslide is 1 km–3.3 km, and the mine is not only high in altitude but also close to rivers, while the Miyun open-pit mine monitoring distance is 0.3 km–1 km, altitude is 158 m, and there is no river around.

3.1. Woda landslide

The Woda landslide is located in Sichuan Province, China, at an altitude of approximately 3550 m. The landslide body is not only high in altitude but also features rivers around the landslide body, which makes the atmospheric flow conditions more complex. It is an ideal experimental site for atmospheric algorithms. As shown in Figure 2, there is obvious deformation in the landslide mass. Three points were selected from the deformation area of the landslide, as presented in Figure 2(a), to examine their temporal evolution. From

Table 1. Monitoring parameters of the two study areas.

	Monitoring range (km)	Altitude (m)	River
Woda landslide	1–3.3	3550 m	√
Miyun open-pit mine	0.3–1	158 m	×

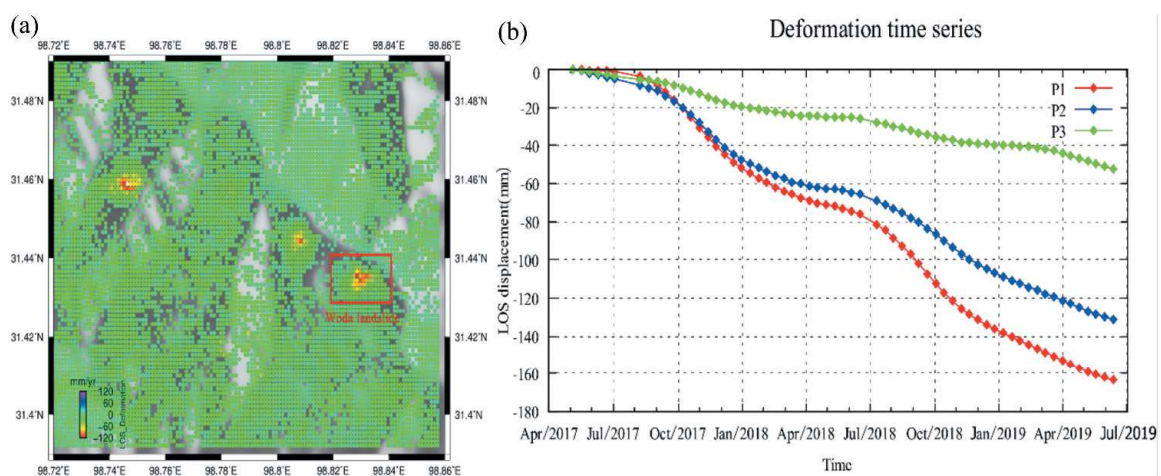


Figure 2. Spaceborne InSAR (Sentinel-1, ascending track 99) from May 2017 to May 2019. (a) Cumulative displacement map. (b) Displacement time series of the three points.

Figure 2(b), point 1 exhibited an approximately -160 mm displacement. The deformation of landslides is closely related to rainfall. In the rainy season, the deformation of landslides accelerates, but there is a lag period of one month. In the dry season, the deformation of landslides is slow.

3.1.1. Deformation data acquisition and processing of the Woda landslide

From 4 July 2019 to 13 July 2019, the authors carried out a discontinuous monitoring campaign using GBR equipment to verify the applicability of the three methods on the Woda landslide considering the safety of the instrument. In this context, a total of seven datasets were sufficient to obtain reliable deformation results (see Table 2) and achieve discrete monitoring of the landslide.

In this study, a GAMMA portable radar interferometer was employed. It can not only produce high spatial (0.75 m in range, 6.8 m in azimuth at 1 km) and temporal resolution (10 s) but can also be deployed flexibly to customize the observation. The GPRI-II was mounted on a stationary concrete base, scanning the landslide at a temporal resolution of 20 minutes. To maximize the sensitivity of the GBR equipment in measuring deformation, the radar's observation vector must be as parallel as possible to the displacement vector. Due to the small elevation difference between the equipment and the landslide, the antenna incidence angle is set to 10 degrees. To encompass the full view of the landslide boundaries, we selected a 40° rotation angle and a 1 km to 3.3 km valid observation distance with respect to the radar (see Table 3). The weather conditions varied dramatically on each of the seven days of data collection. During the same monitoring activity, it could be foggy in the morning, sunny at noon and rainy in the evening. For all the data, the image resolution was set to 3.75 m in the range direction and 3.5 m at 1 km in the

Table 2. Timetable of the measurement campaign.

Campaign	Date	Number of scans
1	20190704120657-20190704200652	25
2	20190705163240-20190706015241	29
3	20190706060332-20190708064331	76
4	20190708134944-20190709124944	70
5	20190709225456-20190710215456	70
6	20190711034954-20190711072954	12
7	20190712030615-20190713020615	70

Table 3. Summary of the main acquisition parameters and data processing parameters for the Woda landslide.

Parameters	Values
Acquisition dates	4 July 2019 ~ 13 July 2019
Effective measurement range	1 ~ 3.3 km
Revisiting times	20 minutes
Incidence	10°
Centre azimuth angle	335°
Azimuth start angle	0°
Azimuth end angle	40°
Coherence threshold	0.6
Multi look (range: azimuth)	5:200
Phase unwrapping	Minimum cost flow

azimuth direction with an image size of 614×199 . For all the campaigns, 352 images were processed within one unit.

An overview of the observed landslide is shown in Figure 3(a). The area marked with the yellow polygon indicates the monitoring area of the landslide, and the point marked with the red star shows the monitoring position. A schematic diagram of the acquired GBR data is displayed in Figure 3(b). The schematic of the proposed strategy is displayed in Figure 4 (Wang et al. 2019). A block dot represents one acquisition, and a rectangle represents a single GPRI-II data campaign. The GBR time series analysis chain is based on the small baseline subset (SBAS) algorithm (Pepe et al. 2005; Hooper 2008; Lauknes et al. 2010).

To improve the calculation efficiency, a new time series estimation method (Davies and Blewitt 2000) should be used. The time series estimation produces an optimal solution within each unit. However, the solution for a unit is not necessarily global when multiple units are required. To solve this issue, nearby units can be linked by their common coherent pixels in the time series. The adjacent units are then merged into a longer unit, and the optimal solution for the whole campaign can be achieved. Because the time series is analysed within each unit independently, the selected coherent pixels in different units may also be different. To ensure an optimal solution for the global unit, all units may be merged into a unit on the basis of the two coherent pixel sets.

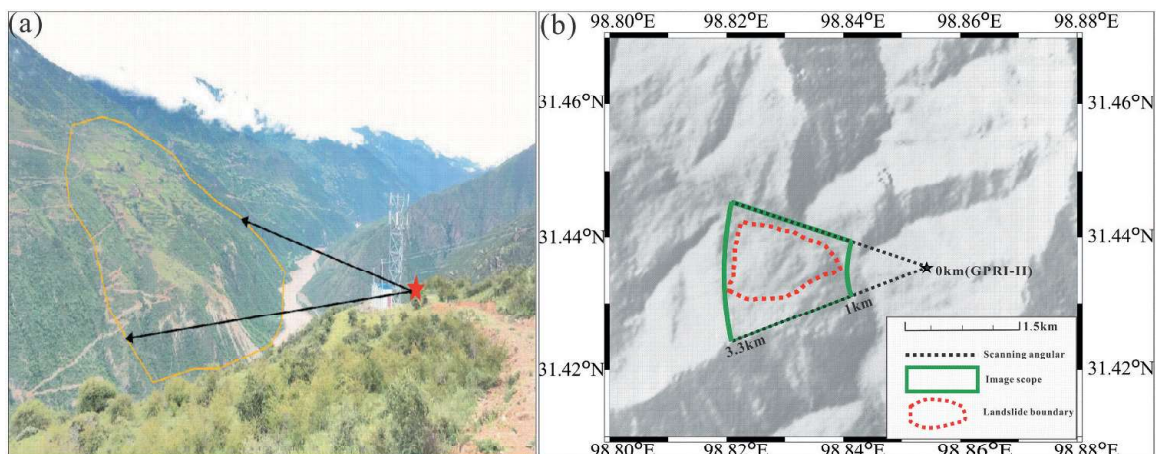


Figure 3. An overview of the observed landslide and schematic diagram of the acquired GBR data. (b) The blue box indicates the image scope of GPRI-II. The red polygon shows the landslide area. The black star indicates the location of the GBR.

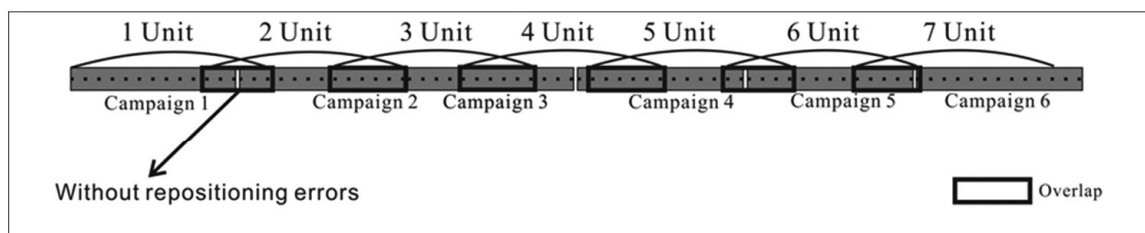


Figure 4. Schematic diagram of the GBR data types. For example, assume two units are defined with a window size of 16 and a temporal baseline constraint of 3 (i.e. overlap size of 6). The first unit runs from the 1st to the 16th image, and the second unit runs from the 11th to the 26th image.

The atmospheric correction process of all the interferograms is given as follows: (1) generation of the interferograms (Wang, Li, and Mills 2018), (2) adaptive estimation of the coherence (Kraut, Scharf, and Butler 2005), (3) selection of coherent pixels (Wang, Zhao, and Liu 2018), (4) non-local filtering of the interferograms (Goldstein and Werner 1998; Chen et al. 2010), (5) phase unwrapping (2D/3D) (Carballo and Fieguth 2000; Costantini et al. 2002), (6) correction of the APS (Noferini et al. 2005; Pipia et al. 2006, 2008; Iannini and Guarnieri 2010; Iglesias et al. 2013; Huang et al. 2015), (7) inversion of the line-of-sight (LOS) displacement, and (8) generation of the displacement maps.

3.1.2. APS correction model results of the Woda landslide

To estimate the GBR performance under varied weather conditions, three datasets were selected, each comprising 2 images. Three GBR parameters were investigated to compare the performance under different weather conditions: amplitude, interferogram, and coherence. The amplitude is the strength of the backscattered electromagnetic signal, which provides information on the reflectivity of the illuminated field. It can be used to interpret the observing scene. The quality of the derived interferograms is the key to successful deformation applications. Coherence is selected, which is the most commonly used indicator of interferometric phase quality (Ferretti, Prati, and Rocca 2001; Eldhuset et al. 2003; Jiang, Ding, and Li 2013). Using the data with 2 continuous images under different periods, the images and coherences are displayed in Figure 5.

It is clear from Figure 5 that during the clear period, the dataset shows high coherence, but the coherence decreases prominently during the monitoring period with fog and rain. The quality and number of coherence pixels are important parameters to estimate the final results. Moreover, they play a key role in the time series analysis.

Statistics including the overall mean coherence and the number of coherent pixels (percentage of the total pixels of the entire image) are summarized in Table 4. As shown in Table 5, the density of coherent pixels in the clear conditions was the highest. This strongly suggests that the interferometric measurement under clear conditions outperforms that conducted under rainy and foggy conditions.

Using the algorithm described in Section 2, the deformation results of GBR are obtained. In this monitoring campaign, a redundant network of interferograms was constructed in which each image was allowed to generate interferograms with the two previous and two subsequent images. In total, 352 images were processed within one unit under different methods, and the results are displayed in Figure 6. Clearly, atmospheric disturbances influence the time series results (Figure 6(a)). We selected 5 points from those whose coherences were > 0.6 for the time series analysis in Figure 7. The maximum deformation reaches 40 mm.

3.2. Miyun open-pit

The Miyun open-pit mine is located in the middle of Miyun District, Beijing, China, which has a warm temperate semi humid continental monsoon climate. The maximum depth of the open pit is -76 m, the stage height is 12 m, and the closed circle is 144 m. The maximum elevation difference of the open pit is 312 m. The internal deformation is likely to be the unstable surface deformation caused by the air flow change in the pit (Figure 8).

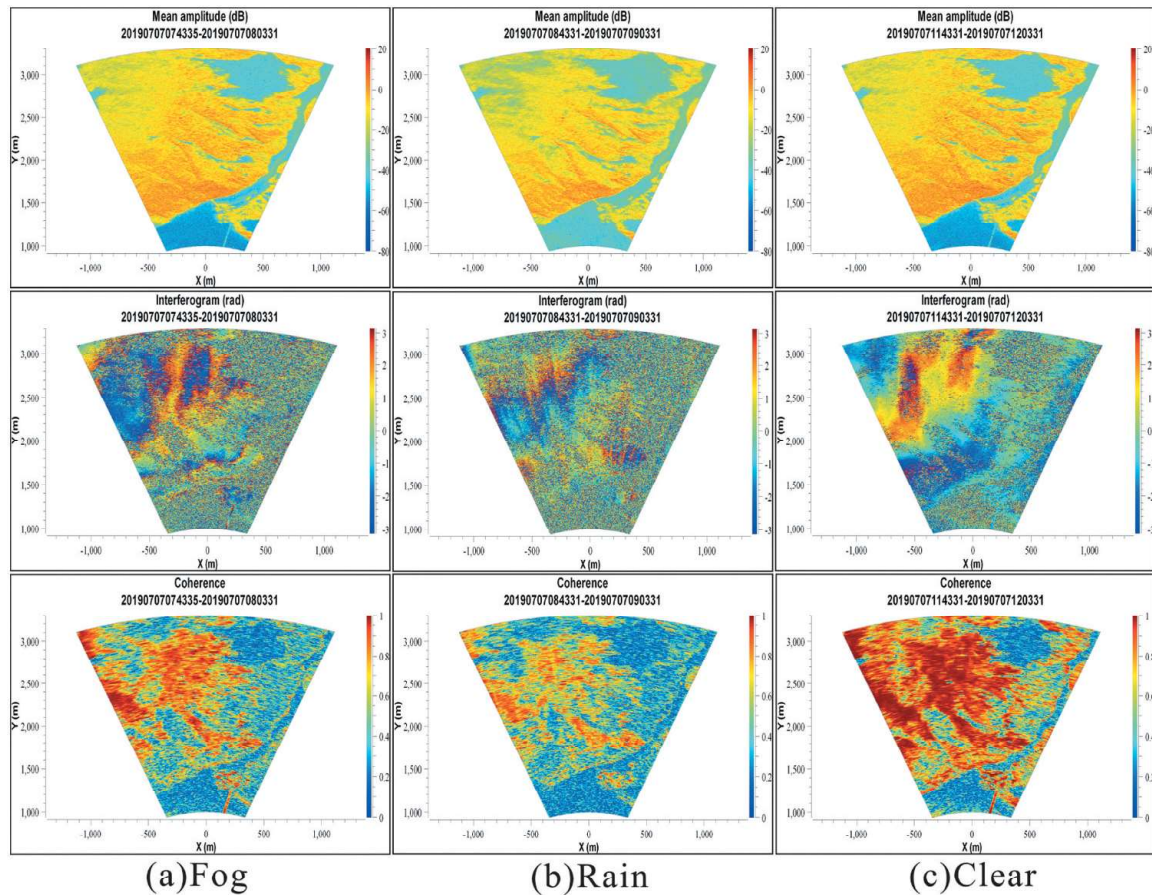


Figure 5. Images and coherences of the GPRI-II data collected under different weather conditions on 7 July 2019. (a) Foggy conditions. (c) Rainy and foggy conditions. (e) Clear conditions.

Table 4. Statistics under different weather conditions.

	Fog	Rain	Clear
Mean coherence	0.29	0.22	0.45
Coherent pixels (>0.6)	38,899 (12.73%)	18,768 (6.14%)	101,748 (33.30%)

Table 5. Summary of the main acquisition parameters and data processing parameters for the Miyun open-pit mine.

Parameters	Values
Acquisition dates	07:21, 18 March 2019 ~ 09:03, March 2019
Effective measurement range	0.3 ~ 1 km
Revisiting times	10 minutes
Incidence	10°
Centre azimuth angle	210°
Azimuth start angle	-50°
Azimuth end angle	40°
Coherence threshold	0.6
Multi look (range: azimuth)	2:82
Phase unwrapping	Minimum cost flow

3.2.1. Deformation data acquisition and processing of the Miyun open-pit mine

The Miyun open-pit mine was a fast-changing case with deformations during monitoring on 18 March 2019. The study site was located in a mining area. Because of artificial mining, the mine is in an unstable state, which allows the occurrence of deformations to be easily

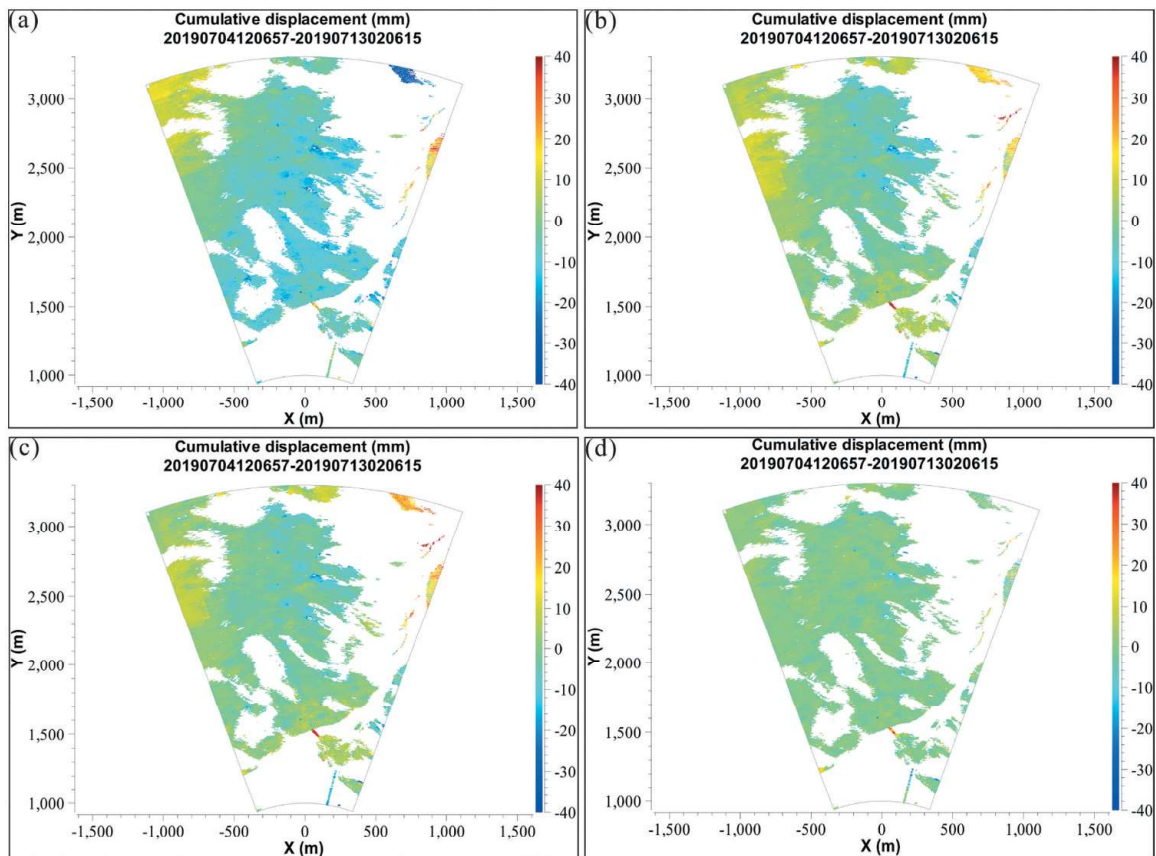


Figure 6. Results of the data collected from 4 July 2019–13 July 2019. (a) Original result. (b) Homogeneous model. (c) Stratified model. (d) ITD. Note that all the maps presented in this paper are subtitled in the format YYYYMMDDHHMMSS.

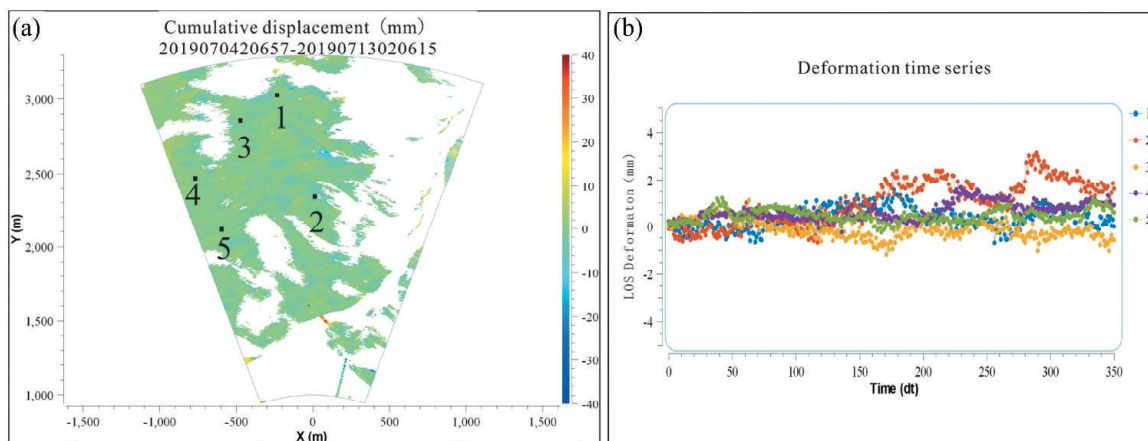


Figure 7. Results of the data collected from 4 July 2019–13 July 2019, including the cumulative displacement and deformation time series.

detected. Twelve images were acquired over one and a half hours on 18 March 2019 by the GPRI-II system, and the imaging parameters of GPRI are shown in Table 5. We use a continuous mode and apply the direct integration method to integrate the 21 interferograms formed by processing each image with the subsequent two.

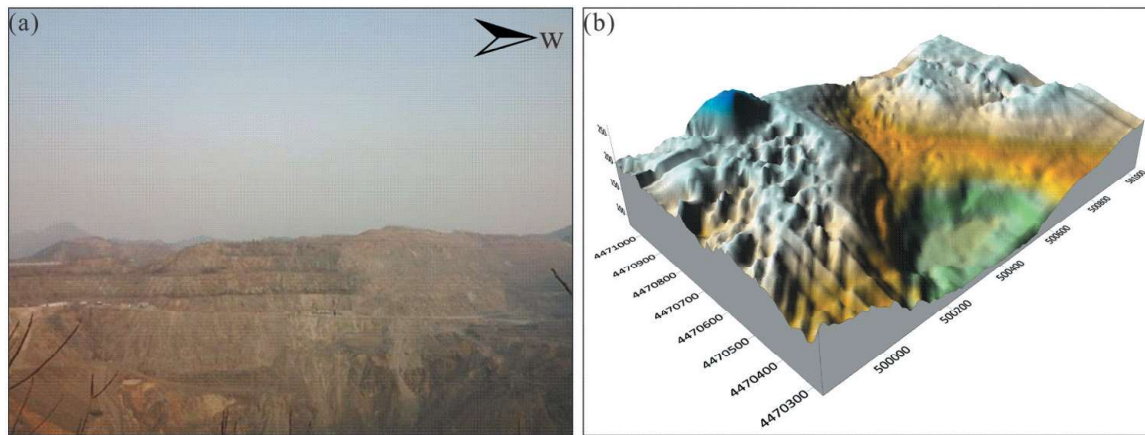


Figure 8. Overview of the Miyun open-pit mine. (a) Site map of the mine. (b) Topographic map of the mine.

3.2.2. APS correction model results of the Miyun open-pit mine

An image and its subsequent three images were used for interferogram generation. The results of the 4 LOS cumulative deformation maps are displayed in Figure 9. It is clear that the range- and/or height-dependent models apply to this case. The phase filtering method fails for short-distance monitoring, and atmospheric refraction is not complex. We select 3 points whose coherences were > 0.6 from the LOS deformation velocity map for the time series analysis in Figure 10. The maximum deformation reaches 4.03 mm. To show the displacement time series, points 1–2 were selected from the deformation area, and point 3 was randomly selected from stable areas. Points 1–2 moved away quickly from the GPRI-II system during the observation period, indicating a sliding process. There is an increasing trend around point 2 towards the radar.

4. Discussion

4.1. Applicability of ITD and range- and/or height-dependent models

If a DEM is available, GPRI-II images can be geocoded easily, and it is convenient for final users to research. The GPRI-II has three antennas (one transmission antenna and two receiving antennas). The antennas are marked TX, RX1 and RX2. The vertical distance is 25 cm between the upper RX1 and lower RX2. The images of the upper RX1 and lower RX2 are obtained synchronously, and the atmospheric phase can be neglected. In the process, many images are required to calculate the average value of the interferogram. The relation between elevation z and phase difference ϕ (Nico et al. 2004; Noferini et al. 2007b; Noferini et al. 2009; Rödelberger et al. 2010) of one particular pixel can be approximated by

$$z = \frac{\lambda \phi r}{4\pi b} \quad (7)$$

where λ is the wavelength, r is the distance to the target and b is the vertical baseline. The generated DEM can be used in stratified and ITD models.

To evaluate the effect of the APS model, root mean square errors (RMSEs) are introduced (Yu, Penna, and Li 2017; Yu, Li, and Penna 2018). RMSEs of the interference phase in

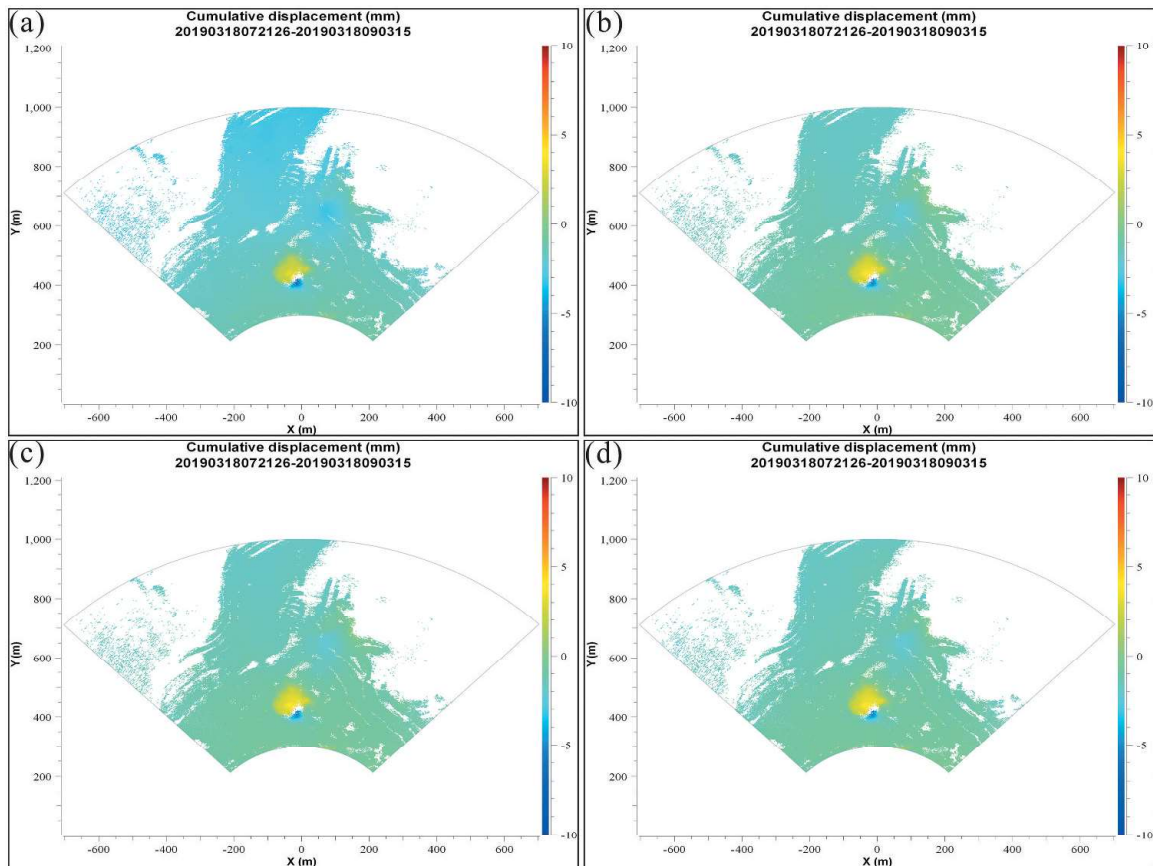


Figure 9. Results of the data collected from 17 March 2019 (a) Original result. (b) Homogeneous model. (c) Stratified model. (d) ITD.

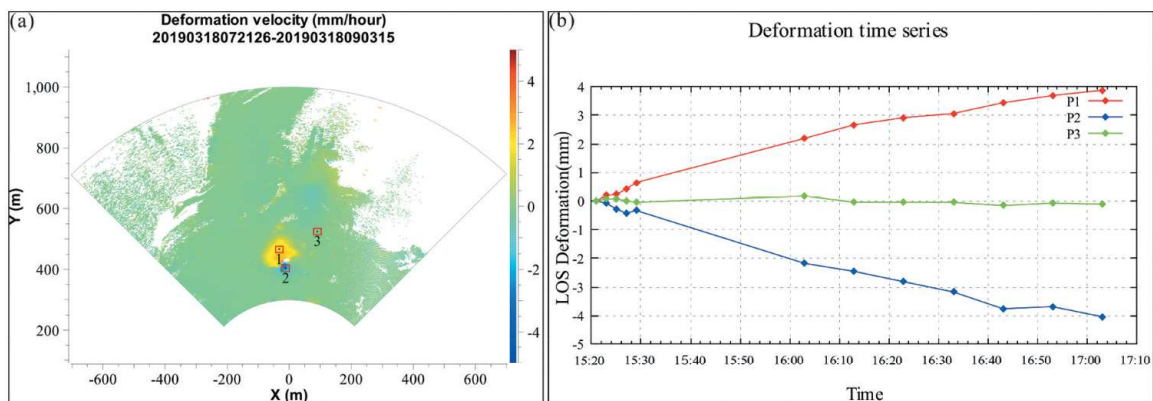


Figure 10. Miyun open-pit mine monitoring results from 18 March 2019, including the deformation velocity and deformation time series.

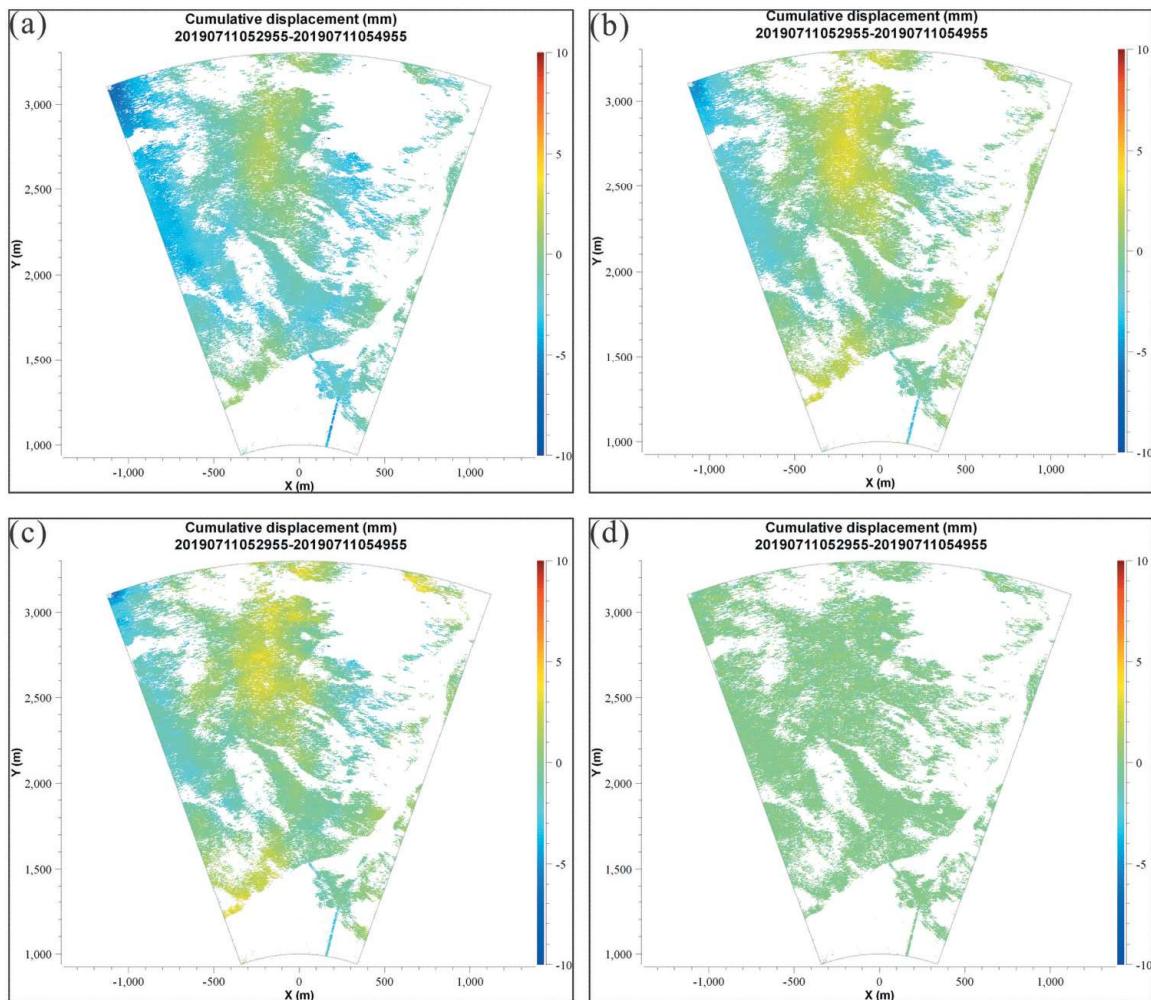
the non-deformable region and the coherent region are calculated to ensure the effect of atmospheric correction. In other words, the smaller the RMSEs are, the better the effectiveness. A pair of different interferometry sets of the Woda landslide and Miyun open-pit mine are selected for study with homogeneous, stratified and ITD models. The RMSEs of the four different interferometry sets for the Woda landslide are 1.36137, 1.36138, 1.2751 and 0.3585 in Table 6. However, the RMSEs of the four different D-InSARs for the Woda landslide are 0.2956, 0.2681, 0.2720 and 0.1412. According to the results in Table 7, the ITD

Table 6. RMSEs of the different APS models for the Woda landslide.

	APS model	RMSEs
Woda landslide	Original result	1.36137
	Homogeneous model	1.36138
	Stratified model	1.2751
	ITD	0.3585

Table 7. RMSEs of the different APS models for the Miyun open-pit mine.

	APS model	RMSEs
Miyun open-pit mine	Original result	0.2956
	Homogeneous model	0.2681
	Stratified model	0.2720
	ITD	0.1412

**Figure 11.** Results of different interferometry analyses with different APS models. (a) The original different interferometry for the Woda landslide. (b-d) The results of different interferometry analyses with homogeneous, stratified and ITD models for the Woda landslide.

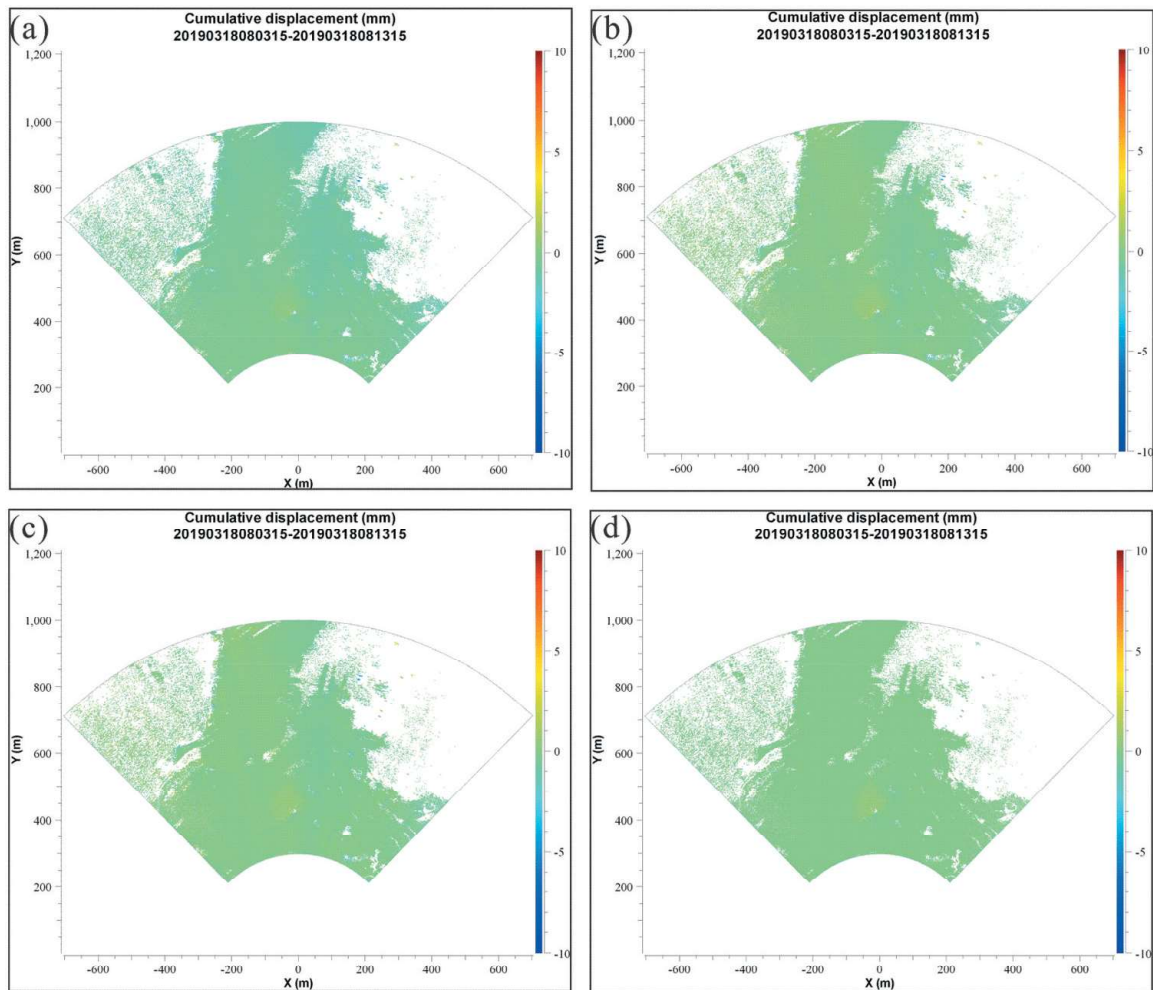


Figure 12. Results of different interferometry analyses with different APS models. (a) The original different interferometry for the Miyun open-pit mine. (b-d) The results of different interferometry analyses with homogeneous, stratified and ITD models for the Woda landslide.

result is very poor when the distance is short and the atmospheric variables are relatively stable, but the result is satisfactory for complex atmospheric conditions.

4.2. Mechanism analysis

From Figures 11 and 12, we find that the effects of the homogenous model and stratified model are not exactly the same in the two study areas. The RMSEs of the standardized model are smaller than those of the homogenous model, which indicates that the effect of the standardized model is more obvious, and Figure 11(b,c) also illustrate this situation. For the Miyun open-pit mine, the homogenous model and stratified model show similar results. This is because the elevation difference of the Miyun open-pit mine is approximately 100 m, while the elevation difference of the Wada landslide is 600 m and the landslide is close to the Jinsha River. Therefore, the effects of the stratified model and homogenous model in the atmospheric phase correction of the Miyun open-pit mine area are very similar.

Compared with ITD and range- and/or height-dependent models, it is found that the effect is good in the research area with a large elevation difference and fast air flow. In locations with a small elevation drop and where the air flow environment is not complex, the ITD method extracts the wavelength of long wave signals from the stratification-corrected interferogram. Therefore, when the threshold of wavelength is set to be large, the ITD method becomes a stratified model, which also shows that the APS in the research area of the Miyun open-pit mine is very poor.

5. Conclusions

This paper mainly analysed the utility of GBR for monitoring landslides and open-pit mines under different APS correction models. For long-distance monitoring with complex atmospheric disturbances, the range- and/or height-dependent models fail. However, the ITD method can effectively address complex atmospheric disturbances. The research indicates that long-distance monitoring under complex atmospheric conditions is suitable with the ITD method. Range- and/or height-dependent models and the ITD method are both effective for short-distance monitoring and simple atmospheric conditions. If the threshold of wavelength is set to be large, the ITD method becomes a stratified model.

Acknowledgements

The Sentinel-1 data are provided by the European Space Agency (ESA) through the Sentinels Scientific Data Hub. Associate Professor Haitao Qian and Tao Li took part in the emergency monitoring of the Woda landslide, and we thank them.

Data availability statement

The Sentinel-1A/B SAR images were downloaded from the Sentinel-1 Scientific Data Hub (<http://scihub.copernicus.eu>).

Disclosure statement

No potential competing interest was reported by the author(s).

Funding

This research was funded by a research grant from the National Institute of Natural Hazards, Ministry of Emergency Management of China [ref. ZDJ2019-17, ZDJ2020-04, ZDJ2018-16]. Part of this work was also funded by the National Natural Science Foundation of China [ref. 41772219, ref. 41704051].

ORCID

Bingquan Li  <http://orcid.org/0000-0002-7211-1899>

Wenliang Jiang  <http://orcid.org/0000-0002-2006-4605>

References

- Butt, J., A. Wieser, and S. Conzett. 2016. "Intrinsic Random Functions for Mitigation of Atmospheric Effects in Ground-Based Radar Interferometry." *Proceedings of JISDM*, 1–9. Vienna: JISDM.
- Caduff, R., A. Kos, F. Schlunegger, B. W. McArdell, and A. Wiesmann. 2014. "Terrestrial Radar Interferometric Measurement of Hillslope Deformation and Atmospheric Disturbances in the Illgraben Debris-Flow Catchment, Switzerland." *IEEE Geoscience and Remote Sensing Letters* 11 (2): 434–438. doi:10.1109/lgrs.2013.2264564.
- Caduff, R., F. Schlunegger, A. Kos, and A. Wiesmann. 2015. "A Review of Terrestrial Radar Interferometry for Measuring Surface Change in the Geosciences." *Earth Surface Processes and Landforms* 40 (2): 208–228. doi:10.1002/esp.3656.
- Carballo, G. F., and P. W. Fieguth. 2000. "Probabilistic Cost Functions for Network Flow Phase Unwrapping." *IEEE Transactions on Geoscience and Remote Sensing* 38 (5): 2192–2201. doi:10.1109/36.868877.
- Chen, J., Y. Chen, W. An, Y. Cui, and J. Yang. 2010. "Nonlocal Filtering for Polarimetric SAR Data: A Pretest Approach." *IEEE Transactions on Geoscience and Remote Sensing* 49 (5): 1744–1754. doi:10.1109/tgrs.2010.2087763.
- Corinthios, M. J. 2003. "Generalized Transforms for DSP and Generalized Spectral Analysis." *Systems Analysis Modelling Simulation* 43 (11): 1433–1462. doi:10.1080/0232929022000002827.
- Costantini, M., F. Malvarosa, F. Minati, L. Pietranera, and G. Milillo. 2002. "A Three-Dimensional Phase Unwrapping Algorithm for Processing of Multitemporal SAR Interferometric Measurements." *IEEE International Geoscience and Remote Sensing Symposium*, 1741–1743. Toronto, ON: IEEE.
- Cressie, N. 1990. "The Origins of Kriging." *Mathematical Geology* 22 (3): 239–252. doi:10.1007/bf00889887.
- Davies, P., and G. Blewitt. 2000. "Methodology for Global Geodetic Time Series Estimation: A New Tool for Geodynamics." *Journal of Geophysical Research: Solid Earth* 105 (B5): 11083–11100. doi:10.1029/2000jb900004.
- Di Pasquale, A., G. Nico, A. Pitullo, and G. Prezioso. 2018. "Monitoring Strategies of Earth Dams by Ground-Based Radar Interferometry: How to Extract Useful Information for Seismic Risk Assessment." *Sensors* 18 (1): 244. doi:10.3390/s18010244.
- Eff-Darwich, A., J. C. Pérez, J. Fernández, B. García-Lorenzo, A. González, and P. J. González. 2012. "Using A Mesoscale Meteorological Model to Reduce the Effect of Tropospheric Water Vapour from DInSAR Data: A Case Study for the Island of Tenerife, Canary Islands." *Pure and Applied Geophysics* 169 (8): 1425–1441. doi:10.1007/s00024-011-0401-4.
- Eldhuset, K., P. H. Andersen, S. Hauge, E. Isaksson, and D. J. Weydahl. 2003. "ERS Tandem InSAR Processing for DEM Generation, Glacier Motion Estimation and Coherence Analysis on Svalbard." *International Journal of Remote Sensing* 24 (7): 1415–1437. doi:10.1080/01431160210153039.
- Ferretti, A., C. Prati, and F. Rocca. 2001. "Permanent Scatterers in SAR Interferometry." *IEEE Transactions on Geoscience and Remote Sensing* 39 (1): 8–20. doi:10.1109/36.898661.
- Goldstein, R. M., and C. L. Werner. 1998. "Radar Interferogram Filtering for Geophysical Applications." *Geophysical Research Letters* 25 (21): 4035–4038. doi:10.1029/1998gl900033.
- Hanssen, R. F. 2001. *Radar Interferometry: Data Interpretation and Error Analysis*. Dordrecht: Springer Science & Business Media.
- Heng, S., and D. Jie. 2013. "The Application Research of IBIS-S Telemetry System on the Deformation Monitoring of Bridge." *Geotechnical Investigation & Surveying* 41 (8): 79–82.
- Herrera, G., J. A. Fernández-Merodo, J. Mulas, M. Pastor, G. Luzi, and O. Monserrat. 2009. "A Landslide Forecasting Model Using Ground Based SAR Data: The Portalet Case Study." *Engineering Geology* 105 (3–4): 220–230. doi:10.1016/j.enggeo.2009.02.009.
- Hooper, A. 2008. "A Multi-Temporal InSAR Method Incorporating Both Persistent Scatterer and Small Baseline Approaches." *Geophysical Research Letters* 35 (16): L16302. doi:10.1029/2008gl034654.

- Huang, Z. S., W. X. Tan, Y. P. Wang, J. P. Sun, P. P. Huang, and Y. N. Yuan. 2015. "Space-Varying Atmospheric Phase Correction in Ground-Based SAR Interferometry." IET International Radar Conference 2015, 1–4. Hangzhou: IET.
- Iannini, L., and A. M. Guarnieri. 2010. "Atmospheric Phase Screen in Ground-Based Radar: Statistics and Compensation." *IEEE Geoscience and Remote Sensing Letters* 8 (3): 537–541. doi:10.1109/lgrs.2010.2090647.
- Iglesias, R., X. Fabregas, A. Aguasca, J. J. Mallorqui, C. Lopez-Martinez, J. A. Gili, and J. Corominas. 2013. "Atmospheric Phase Screen Compensation in Ground-Based SAR with a Multiple-Regression Model over Mountainous Regions." *IEEE Transactions on Geoscience and Remote Sensing* 52 (5): 2436–2449. doi:10.1109/tgrs.2013.2261077.
- Jiang, M., X. Ding, and Z. Li. 2013. "Hybrid Approach for Unbiased Coherence Estimation for Multitemporal InSAR." *IEEE Transactions on Geoscience and Remote Sensing* 52 (5): 2459–2473. doi:10.1109/tgrs.2013.2261996.
- Jung, J., D. J. Kim, and S. E. Park. 2013. "Correction of Atmospheric Phase Screen in Time Series InSAR Using WRF Model for Monitoring Volcanic Activities." *IEEE Transactions on Geoscience and Remote Sensing* 52 (5): 2678–2689. doi:10.1109/tgrs.2013.2264532.
- Kraut, S., L. L. Scharf, and R. W. Butler. 2005. "The Adaptive Coherence Estimator: A Uniformly Most-Powerful-Invariant Adaptive Detection Statistic." *IEEE Transactions on Signal Processing* 53 (2): 427–438. doi:10.1109/tsp.2004.840823.
- Lauknes, T. R., A. P. Shanker, J. F. Dehls, H. A. Zebker, I. H. C. Henderson, and Y. Larsen. 2010. "Detailed Rockslide Mapping in Northern Norway with Small Baseline and Persistent Scatterer Interferometric SAR Time Series Methods." *Remote Sensing of Environment* 114 (9): 2097–2109. doi:10.1016/j.rse.2010.04.015.
- Li, Y., Q. Jiao, X. Hu, Z. Li, B. Li, J. Zhang, W. Jiang, Y. Luo, Q. Li, and R. Ba. 2020. "Detecting the Slope Movement after the 2018 Baige Landslides Based on Ground-Based and Space-Borne Radar Observations." *International Journal of Applied Earth Observation and Geoinformation* 84: 101949. doi:10.1016/j.jag.2019.101949.
- Li, Z. 2005. "Interferometric Synthetic Aperture Radar (Insar) Atmospheric Correction: GPS, Moderate Resolution Imaging Spectroradiometer (MODIS), and InSAR Integration." *Journal of Geophysical Research* 110 (B3): B03410. doi:10.1029/2004jb003446.
- Liebe, H. J. 1985. "An Updated Model for Millimeter Wave Propagation in Moist Air." *Radio Science* 20 (5): 1069–1089. doi:10.1029/rs020i005p01069.
- Liu, H., C. Koyama, J. Zhu, Q. Liu, and M. Sato. 2016. "Post-Earthquake Damage Inspection of Wood-Frame Buildings by a Polarimetric GB-SAR System." *Remote Sensing* 8 (11): 935. doi:10.3390/rs8110935.
- Luzi, G., M. Pieraccini, D. Mecatti, L. Noferini, G. Guidi, F. Moia, and C. Atzeni. 2004. "Ground-Based Radar Interferometry for Landslides Monitoring: Atmospheric and Instrumental Decorrelation Sources on Experimental Data." *IEEE Transactions on Geoscience and Remote Sensing* 42 (11): 2454–2466. doi:10.1109/tgrs.2004.836792.
- Nico, G., D. Leva, G. Antonello, and D. Tarchi. 2004. "Ground-Based SAR Interferometry for Terrain Mapping: Theory and Sensitivity Analysis." *IEEE Transactions on Geoscience and Remote Sensing* 42 (6): 1344–1350. doi:10.1109/tgrs.2004.826556.
- Noferini, L., D. Mecatti, G. Macaluso, M. Pieraccini, and C. Atzeni. 2009. "Monitoring of Belvedere Glacier Using a Wide Angle GB-SAR Interferometer." *Journal of Applied Geophysics* 68 (2): 289–293. doi:10.1016/j.jappgeo.2009.02.004.
- Noferini, L., M. Pieraccini, D. Mecatti, G. Luzi, C. Atzeni, A. Tamburini, and M. Broccolato. 2005. "Permanent Scatterers Analysis for Atmospheric Correction in Ground-Based SAR Interferometry." *IEEE Transactions on Geoscience and Remote Sensing* 43 (7): 1459–1471. doi:10.1109/tgrs.2005.848707.
- Noferini, L., M. Pieraccini, D. Mecatti, G. Macaluso, C. Atzeni, M. Mantovani, G. Marcato, A. Pasuto, S. Silvano, and F. Tagliavini. 2007a. "Using GB-SAR Technique to Monitor Slow Moving Landslide." *Engineering Geology* 95 (3–4): 88–98. doi:10.1016/j.enggeo.2007.09.002.

- Noferini, L., M. Pieraccini, D. Mecatti, G. Macaluso, G. Luzi, and C. Atzeni. 2006. "Long Term Landslide Monitoring by Ground-Based Synthetic Aperture Radar Interferometer." *International Journal of Remote Sensing* 27 (10): 1893–1905. doi:10.1080/01431160500353908.
- Noferini, L., M. Pieraccini, D. Mecatti, G. Macaluso, G. Luzi, and C. Atzeni. 2007b. "DEM by Ground-Based SAR Interferometry." *IEEE Geoscience and Remote Sensing Letters* 4 (4): 659–663. doi:10.1109/lgrs.2007.905118.
- Pepe, A., E. Sansosti, P. Berardino, and R. Lanari. 2005. "On the Generation of ERS/ENVISAT DInSAR Time-Series via the SBAS Technique." *IEEE Geoscience and Remote Sensing Letters* 2 (3): 265–269. doi:10.1109/lgrs.2005.848497.
- Pipia, L., X. Fabregas, A. Aguasca, and C. Lopez-Martinez. 2008. "Atmospheric Artifact Compensation in Ground-Based DInSAR Applications." *IEEE Geoscience and Remote Sensing Letters* 5 (1): 88–92. doi:10.1109/lgrs.2007.908364.
- Pipia, L., X. Fabregas, A. Aguasca, and C. Lopez-Martinez. 2012. "Polarimetric Temporal Analysis of Urban Environments with a Ground-Based SAR." *IEEE Transactions on Geoscience and Remote Sensing* 51 (4): 2343–2360. doi:10.1109/tgrs.2012.2211369.
- Pipia, L., X. Fabregas, A. Aguasca, and J. Mallorqui. 2006. "A Comparison of Different Techniques for Atmospheric Artefact Compensation in GBSAR Differential Acquisitions." 2006 IEEE International Symposium on Geoscience and Remote Sensing, 3722–3725. Denver, CO: IEEE.
- Rödelsperger, S., M. Becker, C. Gerstenecker, G. Läufer, K. Schilling, and D. Steineck. 2010. "Digital Elevation Model with the Ground-Based SAR IBIS-L as Basis for Volcanic Deformation Monitoring." *Journal of Geodynamics* 49 (3–4): 241–246. doi:10.1016/j.jog.2009.10.009.
- Tarchi, D., H. Rudolf, M. Pieraccini, and C. Atzeni. 2000. "Remote Monitoring of Buildings Using a Ground-Based SAR: Application to Cultural Heritage Survey." *International Journal of Remote Sensing* 21 (18): 3545–3551. doi:10.1080/014311600750037561.
- Vincent, S., S. A. J. Francis, and E. B. Rajasingh. 2015. "An Alternate Antenna Array Geometry for a GB-SAR System Used in Landslide Monitoring." *Journal of the Indian Society of Remote Sensing* 43 (4): 761–768. doi:10.1007/s12524-015-0456-2.
- Wang, B. H., C. Y. Zhao, and Y. Y. Liu. 2018. "An Improved SAR Interferogram Denoising Method Based on Principal Component Analysis and the Goldstein Filter." *Remote Sensing Letters* 9 (1): 81–90. doi:10.1080/2150704x.2017.1392633.
- Wang, Z., Z. Li, Y. Liu, J. Peng, S. Long, and J. Mills. 2019. "A New Processing Chain for Real-Time Ground-Based SAR (RT-GBSAR) Deformation Monitoring." *Remote Sensing* 11 (20): 2437. doi:10.3390/rs11202437.
- Wang, Z., Z. Li, and J. Mills. 2018. "A New Approach to Selecting Coherent Pixels for Ground-Based SAR Deformation Monitoring." *ISPRS Journal of Photogrammetry and Remote Sensing* 144: 412–422. doi:10.1016/j.isprsjprs.2018.08.008.
- Wei, Z., H. Qihuan, and Z. Shunying. 2016. "Application of Ground-based SAR in Dam Deformation Monitoring Based on PS Method." *Site Investigation Science and Technology* 1: 5.
- Yu, C., Z. Li, and N. T. Penna. 2018. "Interferometric Synthetic Aperture Radar Atmospheric Correction Using a GPS-Based Iterative Tropospheric Decomposition Model." *Remote Sensing of Environment* 204: 109–121. doi:10.1016/j.rse.2017.10.038.
- Yu, C., N. T. Penna, and Z. Li. 2017. "Generation of Real-Time Mode High-Resolution Water Vapor Fields from GPS Observations." *Journal of Geophysical Research: Atmospheres* 122 (3): 2008–2025. doi:10.1002/2016jd025753.
- Zebker, H. A., P. A. Rosen, and S. Hensley. 1997. "Atmospheric Effects in Interferometric Synthetic Aperture Radar Surface Deformation and Topographic Maps." *Journal of Geophysical Research: Solid Earth* 102 (B4): 7547–7563. doi:10.1029/96jb03804.
- Zhang, B., X. Ding, C. Werner, K. Tan, B. Zhang, M. Jiang, J. Zhao, and Y. Xu. 2018. "Dynamic Displacement Monitoring of Long-Span Bridges with a Microwave Radar Interferometer." *ISPRS Journal of Photogrammetry and Remote Sensing* 138: 252–264. doi:10.1016/j.isprsjprs.2018.02.020.